Heliyon 10 (2024) e34427

Contents lists available at ScienceDirect

Heliyon

journal homepage: www.cell.com/heliyon

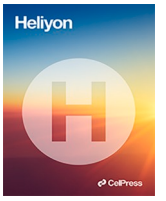

Research article

Investigations of adsorption and photoluminescence properties of encapsulated Al–ZnO nanostructures: Synthesis, morphology and dye degradation studies

Usha Jinendra [a], Sanjay S. Majani [b], Dinesh Bilehal [c,**], B.M. Nagabhushana [d], Y.F. Nadaf [e], Muzaffar Iqbal [f], Chandan Shivamallu [g], Shiva Prasad Kollur [b,*]

[a] Department of Chemistry, The Oxford College of Engineering, Bommasandra, Bangalore, Karnataka, India
[b] School of Physical Sciences, Amrita Vishwa Vidyapeetham, Mysuru Campus, 570 026, Karnataka, India
[c] Department of Chemistry, Karnatak University, Dharwad, 560 008, Karnataka, India
[d] Department of Chemistry, MSRIT, Bengaluru, 560 054, Karnataka, India
[e] Department of Physics, Maharani Cluster University, Palace Road, Bangalore, Karnataka, India
[f] Department of Pharmaceutical Chemistry, College of Pharmacy, King Saud University, Riyadh, 11451, Saudi Arabia
[g] Department of Biotechnology and Bioinformatics, School of Life Sciences, JSS Academy of Higher Education and Research, Mysuru, 570 015, Karnataka, India

ARTICLE INFO

Keywords:
$Zn_{1-x}Al_xO$ nanostructures
Dye degradation
Photoluminescence studies
Solution combustion method

ABSTRACT

This study focuses on the solution combustion approach to examine the nanostructures of undoped and doped ZnO with different concentrations of Al (0.1 % and 0.2 %). Various physical techniques were utilized to characterize the synthesized nanoparticles. X-ray diffraction (XRD) revealed the crystalline materials, while scanning electron microscopy (SEM) with energy-dispersive X-ray (EDX) findings confirmed the products with particle size and the insertion of Al into the ZnO lattice. Fourier-transform infrared spectra (FTIR) confirmed the presence of different functional groups in the obtained material. The results indicate that Al-doped ZnO (Al–ZnO) nanoparticles show promising properties for optoelectronics and photoluminescence. Photoluminescence analysis indicated that an increase in Al3+ (0.2 %) concentration resulted in a decrease in peak intensity and an increase in the full width at half maximum. The band gap was calculated using the Taucs plot. The study also highlights the effectiveness of Zn1-xAlxO nanostructures in degrading organic pollutants, particularly in adsorbing Malachite Green (MG) dye. Among the samples, the 0.2 % Al-doped ZnO exhibited superior dye degradation efficiency due to its enhanced adsorption capacity and smaller particle size, as evidenced by multilayer adsorption capacity and chemisorption during the degradation process. This study provides valuable insights into the potential applications of Al-doped ZnO nanoparticles in various environmental and technological fields, emphasizing their significance in the degradation of organic pollutants.

* Corresponding author.
** Corresponding author.
E-mail addresses: drbilehal@gmail.com (D. Bilehal), shivachemist@gmail.com (S.P. Kollur).

https://doi.org/10.1016/j.heliyon.2024.e34427
Received 26 March 2024; Received in revised form 13 June 2024; Accepted 9 July 2024
Available online 10 July 2024

1. Introduction

Due to its high potential utility in optoelectronics and widespread scientific interest, ZnO has become one of the most heavily investigated metal oxides in recent years. Applications in optoelectronics, nonlinear optics, and electro-optics [1] greatly benefit from the material's high exciton binding energy of 60 meV at room temperature and wide direct band gap of 3.3 eV [2]. Al, a member of group III, easily converts n-type ZnO to p-type ZnO. As an added advantage, ZnO may be used in a number of different. Furthermore, ZnO can be used in various applications, such as gas sensors [3], solar cells [4], and flat panel displays [5]. An obvious advantage of ZnO is that its characteristics can be easily adjusted by manipulating the number of oxygen vacancies within the material. It has been discovered that growth temperature and environment significantly affect ZnO's photoluminescence (PL) characteristics [6]. Stoichiometric ZnO thin films tend to exhibit intense UV fluorescence. Defects such as oxygen interstitials, oxygen vacancies, zinc interstitials, zinc vacancies, and oxide have been proposed as potential causes of green PL [7–10]. Interestingly, when a zinc atom is replaced by an aluminum atom as an extrinsic dopant, the defect environment changes. Therefore, it is important to investigate how doping affects the luminous characteristics of ZnO. Fourier transform infrared (FTIR) spectroscopy utilizes infrared wavelength light to measure a molecule's vibrational energy, albeit in distinct ways. Alterations in the intensity of the spectral band at 437 cm^{-1} (E2 (high) mode of hexagonal ZnO) can serve as an indicator for changes in oxygen content [11]. Al–ZnO can be used to increase the thermoelectric properties under high pressure and temperature [12]. Varudkar et al. (2020) focus on the fabrication of Al–ZnO nanoparticles and their application as a semiconductor-based gas sensor for ammonia detection [13]. Dai et al. (2023) discuss the importance of surface charge recombination in catalysts, which is relevant to the adsorption and degradation capabilities of (Al–ZnO) nanoparticles [14].

Combustion synthesis (CS), also known as self-propagating high-temperature synthesis (SHS), is a cost-effective and useful technique for producing a variety of oxide materials. In recent years, CS has become increasingly popular for the creation of different nanomaterials. The purpose of this study was to synthesize phase-pure Wurtzite structured ZnO phosphor by sintering zinc acetate, zinc nitrate, and ZnO at temperatures of 800 °C, 900 °C, and 1000 °C in a reducing environment for 1 h. It was studied how the photoluminescence (PL) characteristics of ZnO samples are affected by the sintering temperature and how this affects to increase in emission. The ZnO samples sintered in a reducing environment exhibited deep level green fluorescence around 505 nm without the addition of any impurities [15]. Furthermore, this study documents the bulk synthesis of high-quality wurtzite-structured zinc oxide (ZnO) nanoparticles (NPs) using a straightforward wet chemical colloidal technique. The influence of air annealing (up to 800 °C) on the structure, composition, optical properties, and photoluminescence (PL) characteristics of the ZnO nanoparticles was extensively investigated at temperatures up to 800 °C [16]. Another study focused on the impact of Cu doping on the improved UV emission of ZnO nanorods. Through a hydrothermal process, ZnO nanorods with varying levels of Cu doping were successfully synthesized. The results showed that as the concentration of Cu doping increased, the UV emission peak in the PL spectra also increased, while the emission peak in the visible region nearly disappeared [17]. Bentonite-ZnO Nanocomposite Synthesized by Solution Combustion method used for Ciprofloxacin Degradation by photocatalytic activity [18]. The photoluminescence of Li^{+}co-doped polycrystalline sintered ZnO with trivalent rare-earth (RE^{3+}) ions (Dy^{3+}, Er^{3+}, Eu^{3+}, Ho^{3+}, Nd^{3+}, Sm^{3+}, and Tm^{3+}) has been studied [19,20]. The REs doped ZnO have been induced by various methods such as ion implantation [21,22], pulsed laser deposition (PLD) [23], and ultrasonic spray pyrolisis (USP) [24].

The present work describes the synthesis of Al–ZnO nanoparticles using the combustion method. The nanoparticles were doped with Al at concentrations of 0.1 % and 0.2 %. Additionally, this study investigates the photoluminescence of the samples and assesses the degree of dye degradation. The main objective of this research is to determine the structural, optical, and dye degradation properties of Al-doped ZnO nanoparticles.

2. Experimental

2.1. Materials and methods

The precursor chemicals for the preparation of undoped and Al–ZnO nanopowder were zinc acetate dihydrate, aluminum hydroxide and Urea. All the chemicals are of AR grade (purity 99.8 %) and used as received (Merck, US). Using a powder X-ray diffractometer with CuK (1.5406 Å) radiation, the crystallinity of the as-prepared Zn_{1-x} Al_xO was evaluated. The FTIR experiments were run in the 4000 to 400 cm^{-1} range on a Bruker Tensor-27 spectrometer. The Hitachi 3700 NSEM was used to capture the SEM micrographs. Jobin Yvon Fluorolog - FL311 spectrofluorometer was used to record the PL excitation and emission spectra.

2.2. Synthesis of Al–ZnO nanoparticles

Two sets of Al–ZnO nanoparticles were synthesized with varying concentrations of Al dopant: Sample 0.1 % Al–ZnO (Sample 0.1

Table 1
Composition of synthesized Zn_{1-x} Al_xO samples.

Sample (%)	$M^{2+}_{Zn\ (in\ grams)}$	$M^{3+}_{Al\ (in\ grams)}$	$V_{H2O\ (in\ ml)}$
0.1	8.762	0.00624	12.96
0.2	8.714	0.0186	12.92

%), Sample 0.2 % Al–ZnO (Sample 0.2 %): For doping combinations, the molar ratios of urea (1.5 g) were used to determine the composition of the metal oxide. A typical illustration shows the stoichiometric concentration of zinc acetate dihydrate and aluminum hydroxide dissolved in deionized water in a beaker. Then, fuel (urea-1.5 g) was gradually added to the solution while being vigorously stirred for about 10 min. The beaker was placed into a muffle furnace (450 °C) to finish the combustion reaction. The solution undergoes vaporization followed by vigorous ignition with an incandescent flame around 450 °C yielding a voluminous white product that is identified as Zn_{1-x} Al_x O and characterized [25]. The materials used for synthesized samples are listed in Table 1.

3. Results and discussion

3.1. XRD analysis

The X-ray diffraction peaks of $Zn_{1-x}Al_xO$ nanoparticles at different doping levels are depicted in Fig. 1, the powder XRD pattern [25]. Crystalline ZnO solid structure appears to be significantly impacted by the incorporation of Al (secondary phase @ ~38°) [26]. The diffraction peaks match the ZnO nanoparticles reported hexagonal Wurtzite structure as well as the planes (1 0 0), (0 0 2), (1 0 1), (1 0 2), (1 1 0), (1 0 3), (2 0 0), (1 1 2), (2 0 1), and (2 0 2) [27]. Matching with inorganic crystal structure database (ICSD 163382, 182360). Table 2 shows that the lattice parameters a and c dropped as the concentration of Al increased due to the resistance of grain boundaries moving across the secondary phase, such as Al. High levels of Al doping can result in the formation of new phases or secondary phases within the ZnO matrix, which can create additional peaks [28]. Additionally, they can shift the existing peaks towards the higher angle on causing non-uniformity in the strain component [29]. They exerted a delayed force on the grain borders that countered the force driving grain expansion because they knew that this may happen at high Al mol%, which led to a drop in crystallite size [30]. The intensity of the XRD peaks can decrease with higher Al doping levels due to increased disorder and defects within the crystal structure [31].

These findings suggest that raising the Al concentration causes the size of $Zn_{1-x}Al_xO$ nanoparticles to decrease. Therefore, annealing at 450 °C obviously resulted in sharper reflection peaks, showing an increase in crystallinity. After being heated to 450 °C degrees, the crystallite size of $Zn_{1-x}Al_xO$ (x = 0.1 % and 0.2 %) is determined to be 39 nm and 34 nm, respectively. The XRD data may be used to determine the lattice parameters ('a' and 'c'), as $Zn_{1-x}Al_xO$ has a hexagonal unit cell with these above-mentioned values using the following equations [32]:

$$1/d^2 = 4(h^2+k^2+hk)//3a^2+ (l^2/c^2)) \quad (1)$$

Where,

d is the interplanar distance,

$\lambda = 1.54$ Å is the wavelength of the X-ray radiation used [33].

3.2. SEM analysis

Fig. 2 illustrates how smaller particles are produced when the dopant concentration is increased. The average size and form of the nanoparticles are ascertained by SEM analysis of the samples. The XRD and SEM results are in good agreement with the calculated

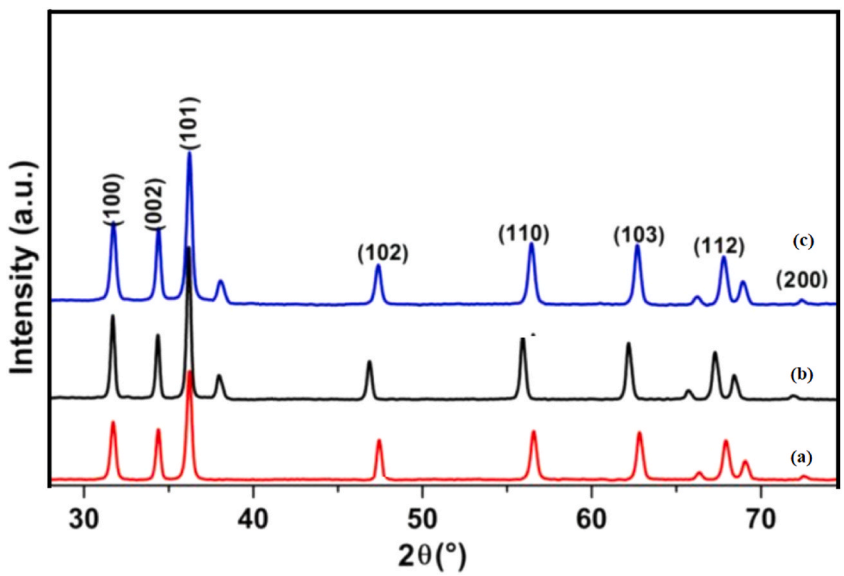

Fig. 1. XRD patterns for (a) ZnO and (b) Zn_{1-x} Al_x O = 0.1 % (c) Zn_{1-x} Al_x O = 0.2 %.

Table 2
The crystallite size and the lattice parameters calculated from diffraction peaks.

Sample	h k l (1 0 1)		Lattice parameters		Scherr formula	
	2θ(°)	D (nm)	a (Å)	c (Å)	Grain size at 38°	strain
ZnO	36.52	41.6	3.25	5.21	29.18 nm	0.0005
0.1 %	36.71	39	2.235	5.20	28.51 nm	0.0013
0.2 %	36.89	34	2.24	5.21	23.76 nm	0.0015

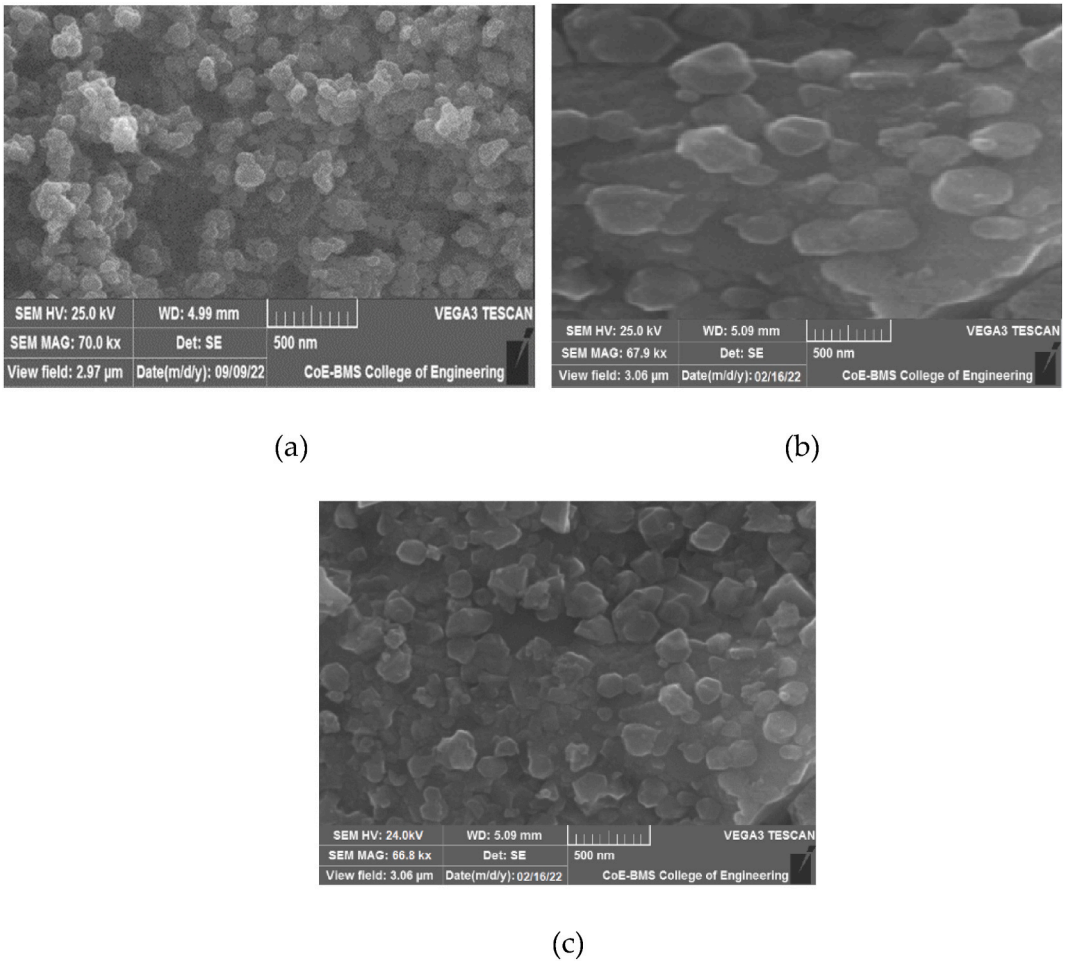

Fig. 2. SEM images of Zn_{1-x} Al_x O nanoparticles: (a) ZnO (b) 0.1 %, (c) 0.2 %.

average particle size using particle size analyzer tool on ImageJ software. Fig. 3 displays the energy dispersive spectra (EDS) of ZnO nanoparticles doped with Al at concentrations of 0.1 % and 0.2 %. The EDX confirms the exceptional purity of the generated $Zn_{1-x}Al_xO$ nanoparticles, showing only the strong peaks of Zn, Al, and O. The Zn characteristic peaks alterations in strength with increasing Al concentration provide more proof that Al^{3+} ions have been replaced in the ZnO lattice [34]. The weight percentage of the respective samples are tabulated in Table 3.

3.3. FTIR analysis

The stretching of a hydroxyl group O–H and bending vibrational absorptions due to water molecules adsorbed on the sample's surface in the environment are represented by the bands at 1620 cm^{-1} and 2250-3600 cm^{-1} (Fig. 4a, b, and 4c). Furthermore, the peaks at 1364 and 1020 cm^{-1} show the lower intensity peaks of the stretching and bending of the vibrational modes for carbonates, which may have happened after boiling the water. The pure ZnO peak at 500 cm^{-1} and 1800 to 800 cm^{-1} is caused by the stretching mode [35,36]. Peaks corresponding to Al–O bonds are expected to appear. These typically manifest in the region around 600–800 cm^{-1}, indicating the presence of aluminum in the ZnO matrix [37]. The frequency of this peak increases with increasing doping levels.

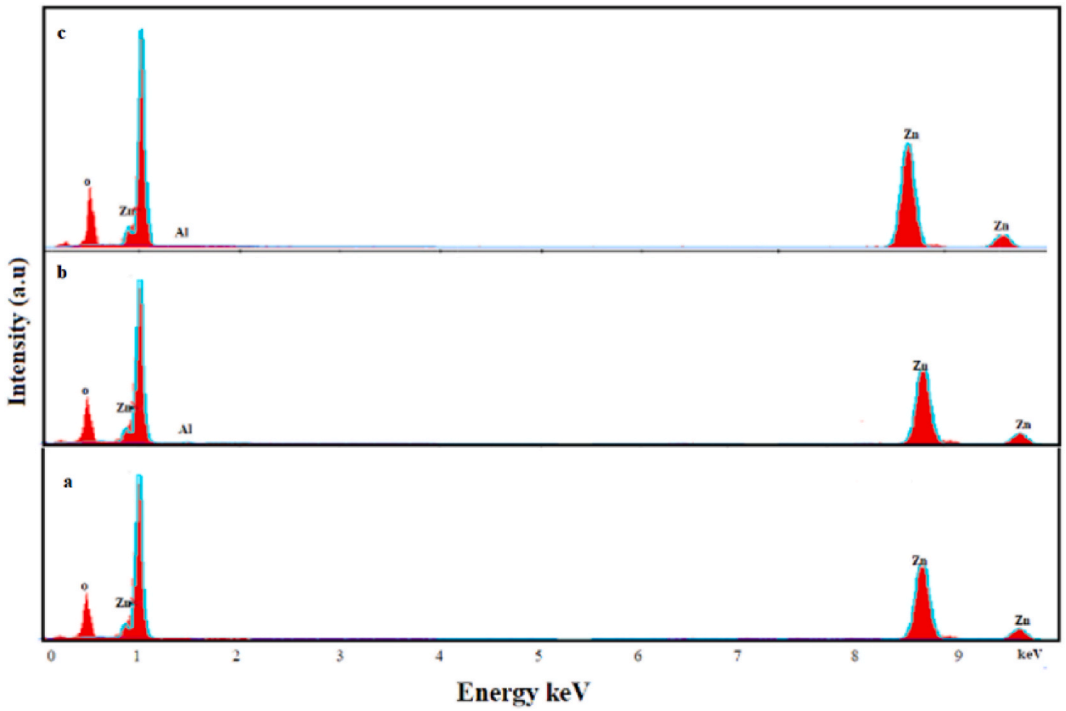

Fig. 3. EDX of (a) Undoped ZnO, (b) Zn_{1-x} $Al_{x\backslash}$ x = 0.1 % and (c) Zn_{1-x} $Al_{x,}$ x = 0.2 %.

Table 3
Atomic weight percentage of respective elements.

Samples	Elements (Weight percentage %)		
	Zn (%)	O (%)	Al (%)
ZnO	80.34	19.66	–
0.1 % Al doped	80.30	19.60	0.1
0.2 % Al doped	80.20	19.60	0.2

This implies that internal strain and the substitution of Al^{3+} ions, which shorten the Zn–O link, are the reasons why ZnO nanocrystallites are becoming smaller. These findings indicate that Zn^{2+} atoms in the ZnO host lattice are being replaced by Al^{3+} ions.

3.4. Photoluminescence investigations

Photoluminescence analysis is crucial for characterizing a variety of material properties. It reveals the lifetime of the excited state and the impurity levels through PL emission. This analysis allows for the communication of both internal and external defects simultaneously [38]. Fig. 5 verifies the energy transfer of electrons from the interstitial to electron transition and from the bottom of the conduction band to the acceptor. This is evident in the characteristic peak at 402 nm. The results demonstrate that as the concentration of Al^{3+} increases, the peak intensity decreases, and the breadth of the half maximum increases. This is attributed to photogenerated electrons in the zinc (Zn^{2+}) conduction band or holes in the valence band undergoing an inter-band radiative combination [39]. The decrease in emission defects in ZnO nanostructures indicates the creation of defect centers through Al doping or the quenching of native defects (Fig. 5). The reported characteristic peak at 402 nm falls within the UV range and represents the near-band-edge emission of ZnO. However, it does not explicitly mention a green emission peak. The absence of this peak in the reported PL spectra could be attributed to several factors: a low concentration of such defects [38], doping defects [39], synthesis method [40], and annealing effects [38].

3.5. Optical absorption spectra/UV absorption spectra

An UV–Vis spectrophotometer operating at room temperature was used to capture the optical absorption spectra of $Zn_{1-x}Al_xO$ (x = 0, 0.1 %, 0.2 %) samples, as shown in Fig. 6a. The absorption edges of each synthesized sample were observed between 300 and 400 nm. The data suggests the presence of mild red shifts in the produced nanoparticles. Furthermore, a red shift in the band gap (Fig. 6b) indicates improved crystallinity in the synthesized samples (0.2 %). The detailed band gap calculation is provided in the

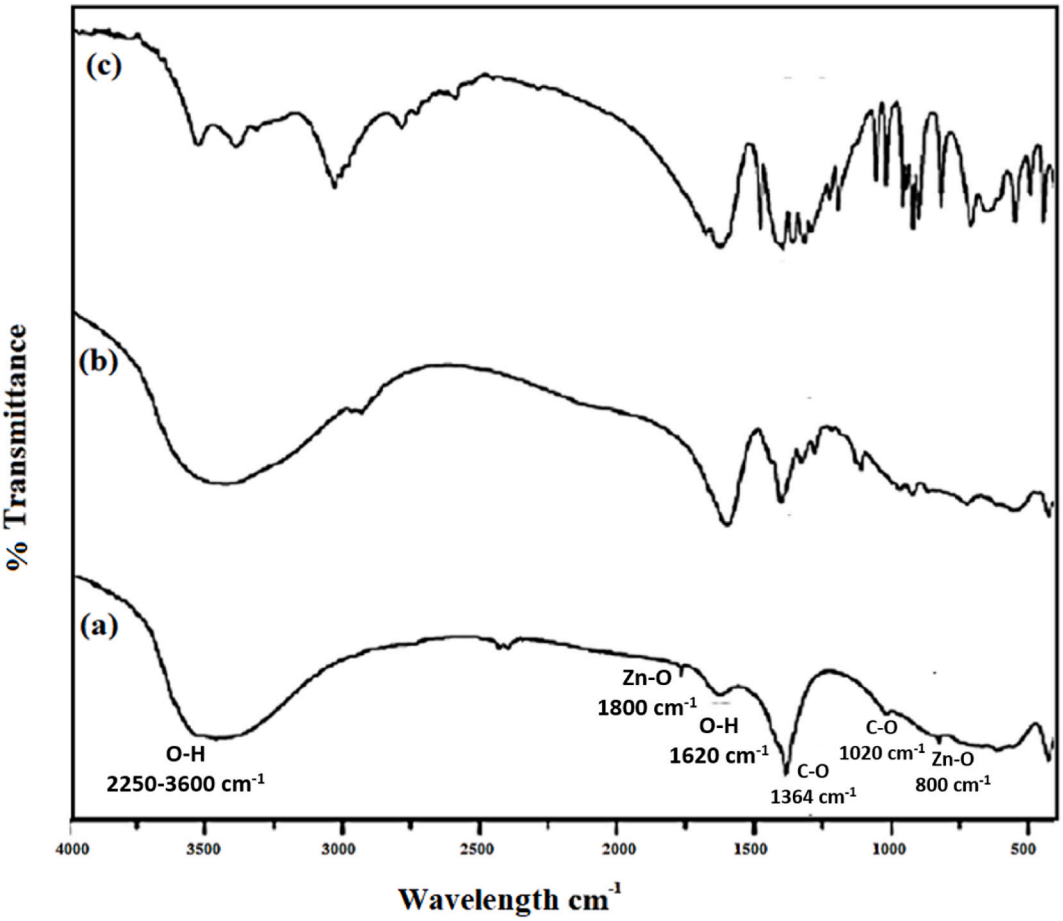

Fig. 4. FT-IR spectra of the as-obtained (a) ZnO and (b) 0.1 % Al–ZnO (c) 0.2 % Al–ZnO.

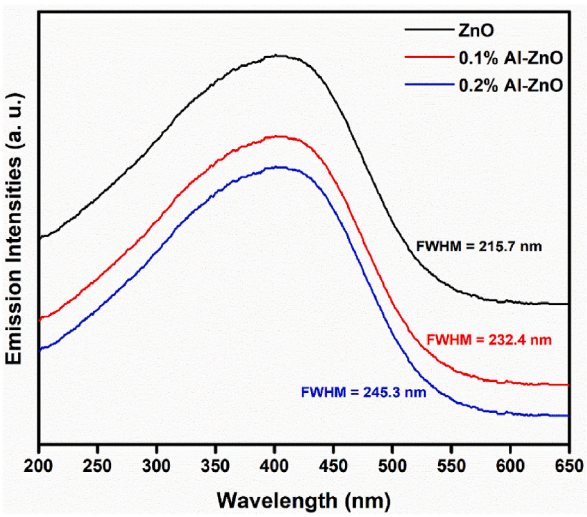

Fig. 5. PL spectra for undoped and two different concentrations of Al doping ZnO.

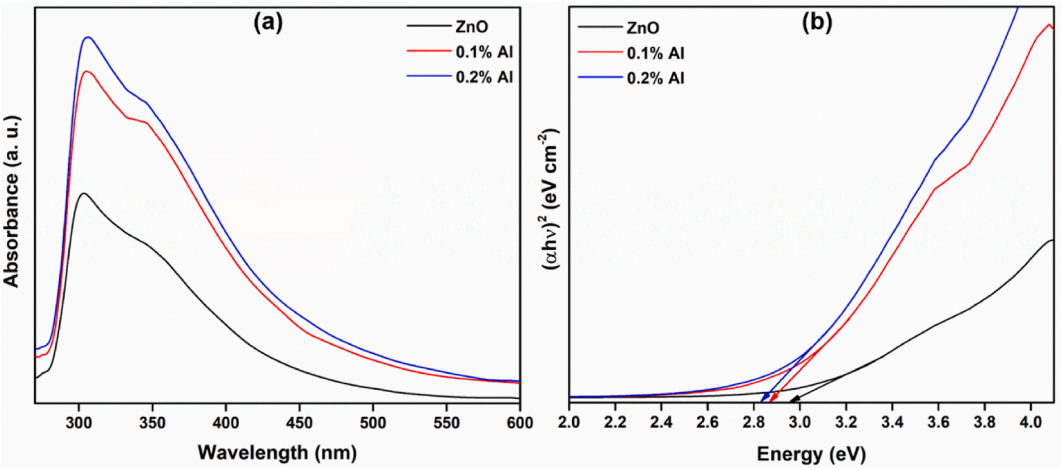

Fig. 6. (a) UV absorption spectra of ZnO nanoparticles doped with 0.1 % and 0.2 % of Al concentration. (b) Band gap evaluation of the respective spectra.

supplementary information.

3.6. Transmission spectra

The optical characteristics of ZnO nanostructures synthesized by solution combustion and ZnO nanostructures doped with Al were assessed using transmission spectroscopy [41]. The treated materials have yielded transmission spectra in the UV–visible range, as Fig. 7 illustrates. The results indicate that the band-to-band absorption edge shifts to a longer wavelength as the dopant concentration increases, with the exact band-to-band absorption edge occurring between 370 and 460 nm.

The calculated band gap energies were 3.15 and 3.19 eV for the concentrations of 0.1 % and 0.2 %, respectively. These band gap energies of ZnO align well with the values previously reported [42]. When plotting the band gap $(\alpha h\nu)^2$ against photon energy ($h\nu$), the band gap is depicted in Fig. 8. According to structural studies, the introduction of Al into ZnO results in structural flaws or lattice damages, causing the energy level to decrease significantly below the conduction band and leading to a decrease in the band gap energy. The presence of lattice faults in ZnO is directly correlated with the concentration of Al, as indicated in Ref. [43].

3.7. CIE chromaticity

Fig. 9 displays the (x, y) parameters from the Commission Internationale de l'eclairage (CIE) that were measured using color gamut space coordinates. The CIE diagram was constructed using the emission spectra of ZnO and Zn1-xAlxO nanoparticles, which have a central wavelength of 402 nm. Each color within the visible spectrum is assigned coordinates (x, y) and is represented by a horseshoe-shaped region on the CIE diagram. The blue emission is distinct in both samples, with the blue region corresponding to their colorimetric (x, y) coordinates [44].

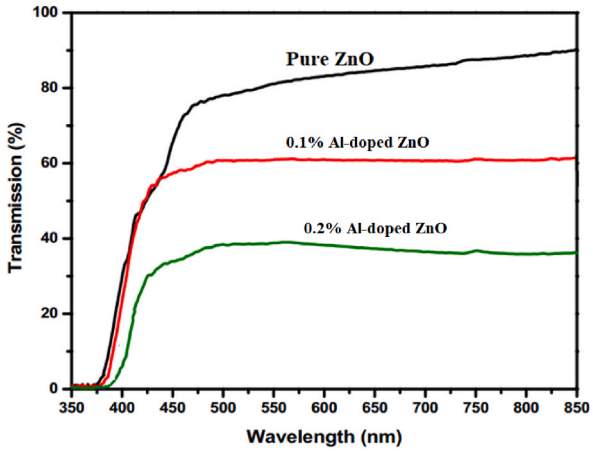

Fig. 7. Transmission spectra of pure ZnO and Al doped ZnO with varying Al concentration.

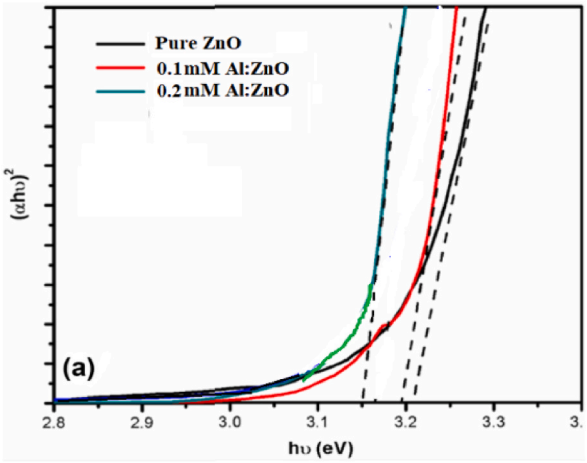

Fig. 8. Plot of $(\alpha h\nu)^2$ vs $h\nu$ of Al:ZnO samples for the calculation of band gap energy.

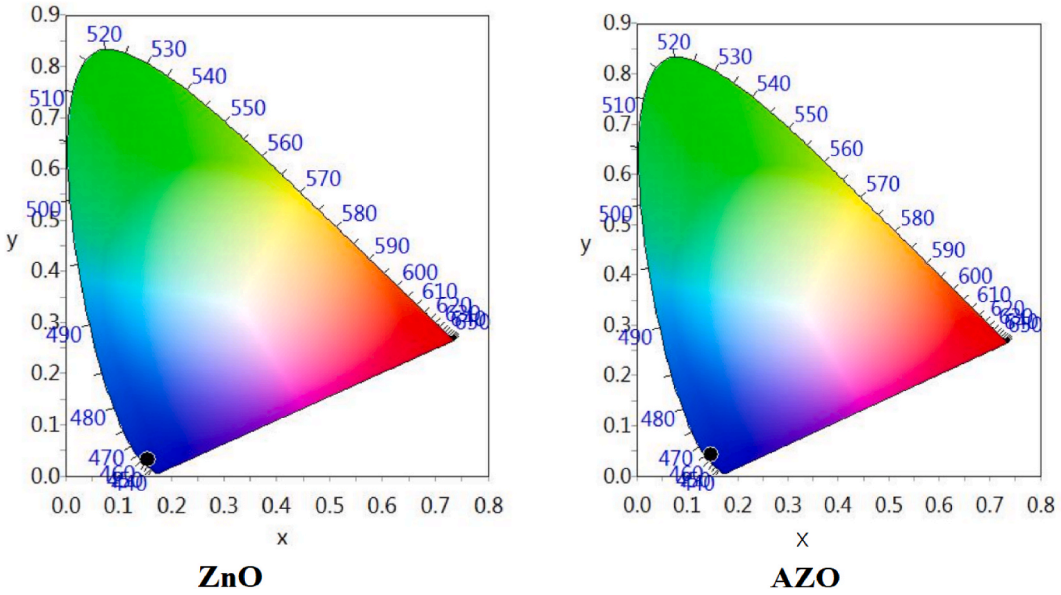

Fig. 9. CIE diagram of pure ZnO and Al–ZnO.

3.8. Zeta potential

Fig. 10 presents the results of measuring the zeta potential and isoelectric point of Al–ZnO heated in water. The Figure provided is slightly higher than the pH_{pzc} value discovered in this inquiry [45]. Greater adsorptive degradation would result from higher dye absorption due to the positively charged Al–ZnO surface and the negatively charged MG dye molecules. Considering the particle size and pH_{pzc} values, it is expected that the Al–ZnO sample will have a higher adsorption capability.

3.9. Effect of different catalyst dosage on MG dye degradation efficiency

Using a wastewater sample containing MG dye, the degradation efficiency of pure ZnO and Al–ZnO nanoparticles (0.1 % and 0.2 %) was investigated. In this experiment, the effects of different dosages and concentrations of ZnO catalysts doped with aluminum were investigated for 10 min. Fig. 11 shows the degradation of wastewater at various catalyst weights (ranging from 1 to 10 mg). 0.2 % Al–ZnO degrades more quickly than 100 % MG at a catalyst concentration of 10 mg. The impact of deterioration rises with catalyst weight and duration, as Fig. 11 demonstrates quite clearly. The results show that because ZnO doped with aluminum (0.2 %) is smaller than both undoped ZnO and ZnO doped with aluminum (0.1 %), it performs better.

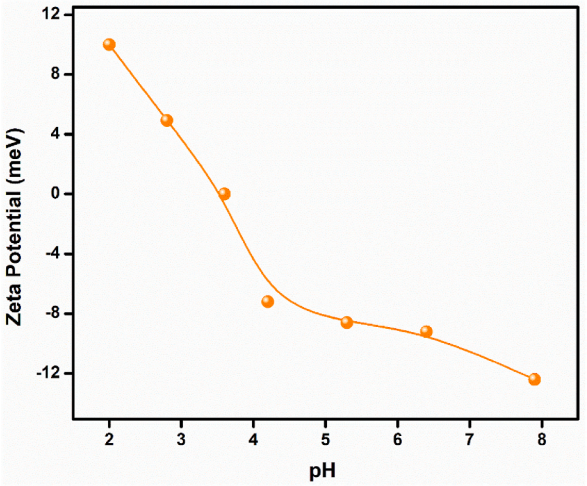

Fig. 10. Effect of zeta potential on Malachite Green (MG) dye degradation. (For interpretation of the references to color in this figure legend, the reader is referred to the Web version of this article.)

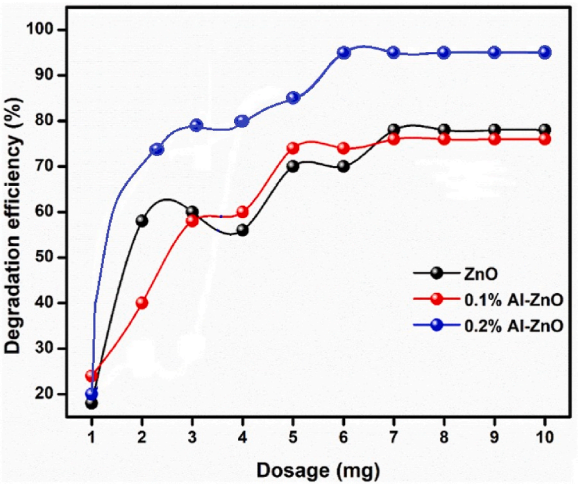

Fig. 11. Effect of adsorbent dosage on Malachite Green (MG) dye degradation. (For interpretation of the references to color in this figure legend, the reader is referred to the Web version of this article.)

3.10. Effect of dye concentration

The effect of the dye concentration varies from 1 to 10 mg/L. Fig. 12 shows that increasing the dye concentration from 1 mg/L to 8 mg/L results in a significant increase in MG adsorption. The abundance of adsorbent sites, which encourage greater surface accessibility and adsorption, may be the cause of this. Nonetheless, there is little difference in elimination efficiency over a dye concentration of 8 mg/L. Reduced adsorption at the conclusion of the experiments suggests the absence of active sites once equilibrium has been reached [46]. Consequently, it has been determined that the optimal dye concentration dose is 8 mg/L, at which point approximately 95 % MG adsorption is achieved. The result shows that Al–ZnO (0.2 %) is more efficient than both 0.1 % and undoped ZnO crystals due to its smaller particle size.

3.11. Effect of contact time on dye degradation efficiency

With varying contact times (ranging from 1 to 9 min), Fig. 13 shows how well the adsorbent performs in relation to MG dye. The adsorption of dyes rapidly increased and then gradually decreased prior to achieving equilibrium. Maybe there are originally as many active sites as possible, and ultimately, they achieve saturation. That would explain this. Occupying the residual empty surface sites is challenging because to the repulsive force generated by the adsorbate (MG) on the solid surface of the adsorbent and the adsorbate (MG) in the bulk phase (solutions). This topic has been the subject of numerous literature reports [47–49]. MG required 4 min of

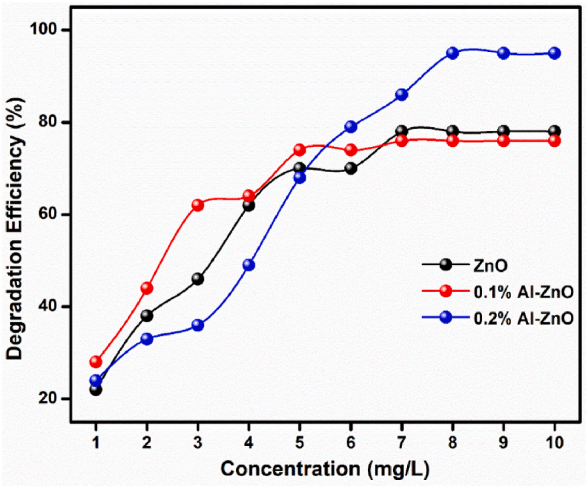

Fig. 12. Effect of dye concentration on the surface of ZnO and Al–ZnO nanoparticles (0.1 and 0.2 %).

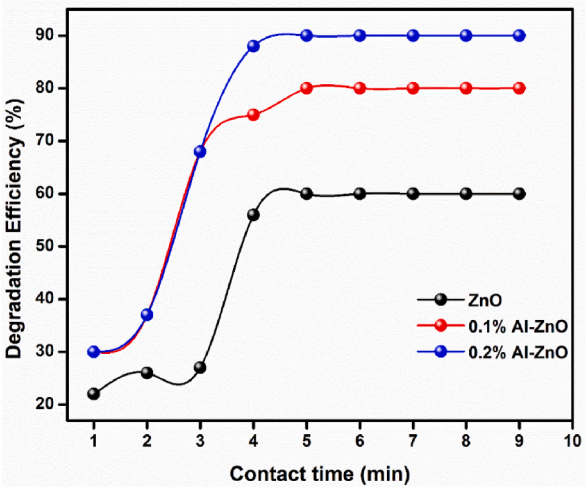

Fig. 13. Effect of contact time on MG dye.

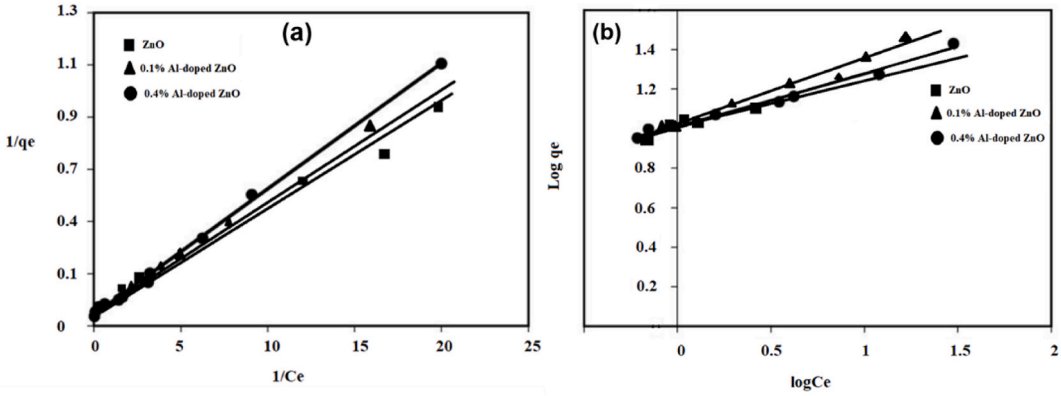

Fig. 14. Experimental data analysis and adsorption equilibrium description showing (a) Langmuir isotherm and (b) Freundlich isotherm.

contact time to attain equilibrium with 95 % removal efficiency, as shown in Fig. 13. As demonstrated by the result, the material's equilibrium time suggests that the adsorbent has an adequate number of active sites for a supplied concentration. From the perspective of the water treatment process, a shorter equilibrium period could be rather advantageous. The findings show that 0.2 % Al–ZnO is more efficient than 0.1 % Al-doped or undoped ZnO. Since 0.2 % Al–ZnO nanoparticles have a tiny particle size, maximum degradation was obtained with them.

3.12. Adsorption isothermal studies

In order to optimize adsorption systems, it is essential to understand the relationship between pollutants and adsorbent materials, which is defined by adsorption parameters and equilibrium data (sometimes referred to as adsorption isotherms). The equilibrium connection between sorbent and sorbate is explained by solubility isotherms, which are often defined as the ratio of the amount adsorbed to the amount left in solution at a fixed temperature [50]. Analysis of experimental data and description of adsorption equilibrium have led to the development of many isotherm models. The dye MG's equilibrium isotherm for adsorption onto an adsorbent was discovered (Fig. 14a). Langmuir, Freundlich and Temkin models are midst explaining solid-liquid sorption systems. The adsorption capacity and dye concentration in the solution were calculated as per the literature.

The Langmuir model adopts that the highest adsorption takes in the monolayer of dye primarily on the adsorbent surface and that all the sites have least interaction between adsorbed molecules and the nanomaterial with similar energy. The Freundlich adsorption isotherm is a practical model which can be used in heterogeneous surface system. Table 4 displays the correlation coefficient, or R^2, values for MG adsorption data that are unmistakably fit by the Freundlich isotherm (Fig. 14b). According to this observation, multilayer adsorption occurs at the surface of the adsorbent's homogeneous binding sites [51].

3.13. Kinetics study

To determine which of the two well-known kinetic models better fits the gathered experimental data, an evaluation is conducted [52]. The following pseudo-first-order rate equation was applied for handling kinetic data.

$$\mathrm{Log}(q_e\text{-}q_t) = \log q_e\text{-}k_1 t/2.303 \quad (2)$$

where q_t and q_e as the quantity adsorbed at time t and at the equilibrium time (mg/g), and the pseudo-first-order rate constant (k_1) for the adsorption process (min^{-1}), respectively. Here is method to express the pseudo second-order model:

$$t/qt = 1/k_2 q^2\ e + (1/q_e)t \quad (3)$$

in which case k_2 (g/mg min) is the pseudo second-order rate constant. From the graph, it can be clear seen that ln (q_e-q_t) against time, and t/q_t against time, respectively.

Fig. 15 depict the pseudo 1st and 2nd order of MG dye, respectively. Comparing pseudo-first order adsorption with second order adsorption yields R^2 (Table 5). The results indicate that the process of adsorption is chemisorption.

4. Conclusion

To sum up, we have emphasized the applicability of the solution combustion method for the synthesis of undoped ZnO nanostructures as well as those doped with Al at 0.1 % and 0.2 % concentrations. The investigation demonstrates the potential photoluminescence and optoelectronic properties of the Al–ZnO nanoparticles. The effectiveness of these nanoparticles in degrading organic pollutants, particularly MG dye adsorption, is another area of attention for the research. The 0.2 % Al–ZnO sample outperforms the 0.1 % and undoped ZnO samples in terms of effectiveness due to its enhanced adsorption capacity and smaller particle size, as per the results. The study also clarifies the optical and structural properties of the nanoparticles, including their absorption spectra, band gap energy, and lattice defects. In conclusion, the finding highlights the versatility of Al–ZnO nanoparticles in both technological and environmental contexts, making them advantageous for the efficient breakdown of organic pollutants.

CRediT authorship contribution statement

Usha Jinendra: Writing – original draft, Methodology, Formal analysis, Conceptualization. **Sanjay S. Majani:** Software, Methodology, Formal analysis, Data curation. **Dinesh Bilehal:** Writing – review & editing, Supervision. **B.M. Nagabhushana:** Visualization, Validation, Methodology, Investigation. **Y.F. Nadaf:** Visualization, Validation, Software, Resources. **Muzaffar Iqbal:**

Table 4
Isothermal parameter of MG dye.

Nanomaterials	Langmuir isotherm	Freundlich isotherm
ZnO	$R^2 = 0.57$	$R^2 = 0.99$
0.1 % Al–ZnO	$R^2 = 0.66$	$R^2 = 0.99$
0.2 % Al–ZnO	$R^2 = 0.69$	$R^2 = 0.99$

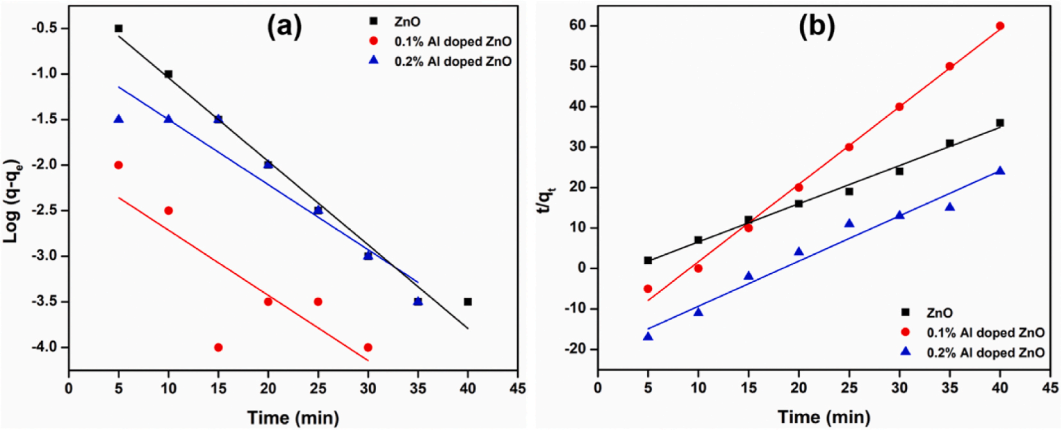

Fig. 15. (a) Pseudo first order kinetics and (b) Pseudo Second order kinetics.

Table 5
Kinetic Parameter of MG dye.

Nanomaterials	Pseudo 1st order	Pseudo 2nd order
ZnO	$R^2 = 0.98$	$R^2 = 0.99$
0.1 % Al–ZnO	$R^2 = 0.89$	$R^2 = 0.99$
0.2 % Al–ZnO	$R^2 = 0.80$	$R^2 = 0.99$

Visualization, Validation, Project administration, Methodology. **Chandan Shivamallu:** Writing – review & editing, Resources, Data curation. **Shiva Prasad Kollur:** Writing – review & editing, Supervision, Project administration, Conceptualization.

Declaration of competing interest

The authors declare that they have no known competing financial interests or personal relationships that could have appeared to influence the work reported in this paper.

Acknowledgements

The authors are thankful to BMSIT, Bengaluru and to the Institute of Excellence, Vijnana Bhavana, University of Mysore, Manasagangotri, Mysuru for providing instrumentation facilities. SPK thank the Director, Amrita Vishwa Vidyapeetham, Mysuru for laboratory facility. The authors extend their appreciation to "Researchers Supporting Project number (RSPD2024R734), King Saud University, Riyadh, Saudi Arabia" for financial support.

Appendix A. Supplementary data

Supplementary data to this article can be found online at https://doi.org/10.1016/j.heliyon.2024.e34427.

References

[1] H.-Q. Liu, C.-B. Yao, G.-Q. Jiang, Y. Cai, Synthesis, structure and ultrafast nonlinear absorption properties of ZnO-time/MoS2 films, J. Alloys Compd. 847 (2020) 156524, https://doi.org/10.1016/j.jallcom.2020.156524.
[2] Y. Sato, K. Kaminaga, R. Takahashi, S. Maruyama, Y. Matsumoto, Impact of band-gap graded structures artificially implemented in Mg–ZnO epitaxial films on photoelectrochemical properties, Catal. Sci. Technol. 12 (21) (2022) 6458–6464, https://doi.org/10.1039/D2CY01178F.
[3] Y. Kang, F. Yu, L. Zhang, W. Wang, L. Chen, Y. Li, Review of ZnO-based nanomaterials in gas sensors, Solid State Ionics 360 (2021) 115544, https://doi.org/10.1016/j.ssi.2020.115544.
[4] A. Wibowo, M.A. Marsudi, M.I. Amal, M.B. Ananda, R. Stephanie, H. Ardy, L.J. Diguna, ZnO nanostructured materials for emerging solar cell application, RSC Adv. 10 (70) (2020) 42838–42859, https://doi.org/10.1039/D0RA07689A.
[5] W. Zhao, S. Bi, L.-h. Chen, K. Asare-Yeboah, J.-h. Song, Ultraviolet-sensitive OLED with tunable wavelength and intensity by integrated ZnO nanowires Schottky junction, Adv. Opt. Mater. 10 (20) (2022) 2201074, https://doi.org/10.1002/adom.202201074.
[6] S. Cho, Synthesis and luminescent properties of Eu^{3+}-doped ZnO phosphors, J. Kor. Phys. Soc. 66 (10) (2015) 1559–1563, https://doi.org/10.3938/jkps.66.1559.

[7] S.D. Birajdar, A.R. Saraf, A.P. Maharolkar, K.P. Gattu, N.G. Patil, R.B. Chavan, M.V. Jamkar, Y.S. Mundhe, R.N. Kambale, R.C. Alange, S.P. Yadav, Intrinsic defect-induced magnetism and enhanced photocatalytic activity in $Zn_{1-x}Zr_xO$ ($0.0 \leq x \leq 0.07$) nanoparticles for spintronic device and photocatalytic application, J. Alloys Compd. 929 (2022) 167272, https://doi.org/10.1016/j.jallcom.2022.167272.

[8] P.S. Menon, M.P. Anjana, A.K. Jose, J. Kunjumon, A. P A, S. Chandran, M. George, G. Vinitha, D. Sajan, The role of defects on linear and nonlinear optical properties of pristine and nickel doped zinc oxide nanoparticles, Surface. Interfac. 34 (2022) 102393, https://doi.org/10.1016/j.surfin.2022.102393.

[9] S. Kaya, O. Ozturk, L. Arda, Correlation between crystal defects and room temperature ferromagnetism of hydrothermally grown Eu substituted ZnO nanorods, Phys. B Condens. Matter 645 (2022) 414281, https://doi.org/10.1016/j.physb.2022.414281.

[10] A. Anjum, R. Ahmed, Z.A. Umar, S. Azzam, T. Hussain, M.N. Sarwar, M.A. Baig, Structure and defects-related optical properties of highly (002)-oriented zinc oxide thin films, Phys. B Condens. Matter 644 (2022) 414195, https://doi.org/10.1016/j.physb.2022.414195.

[11] J.M. Calleja, M. Cardona, Resonant Raman scattering in ZnO, Phys. Rev. B 16 (8) (1977) 3753–3761, https://doi.org/10.1103/PhysRevB.16.3753.

[12] Q. Chen, X. Li, Y. Wang, J. Wang, L. Chang, Y. Zhang, H. Ma, X. Jia, Optimization of thermoelectric properties of Al-doped $Zn_{1-x}Al_xO$ under high pressure and high temperature, J. Alloys Compd. 886 (2021) 161200, https://doi.org/10.1016/j.jallcom.2021.161200.

[13] H.A. Varudkar, G. Umadevi, P. Nagaraju, J.S. Dargad, V.D. Mote, Fabrication of Al-doped ZnO nanoparticles and their application as a semiconductor-based gas sensor for the detection of ammonia, J. Mater. Sci. Mater. Electron. 31 (15) (2020) 12579–12585, https://doi.org/10.1007/s10854-020-03808-7.

[14] Y. Dai, G. Xie, X. Jia, B. Guo, J.R. Gong, Surface charge recombination matters for single-versus polycrystalline catalysts in the case study of hematite photoanodes, Appl. Surf. Sci. 610 (2023) 155501, https://doi.org/10.1016/j.apsusc.2022.155501.

[15] V. Sivakumar, D. Sivaganesh, J.N. Gopal, M. Muthuvinayagam, J.M. Kim, P.K. Kannan, S. Saravanakumar, Enhancement of intrinsic green emission in phase pure ZnO, Phys. B Condens. Matter 644 (2022) 414155, https://doi.org/10.1016/j.physb.2022.414155.

[16] P. Kumari, A. Srivastava, R.K. Sharma, A. Saini, D. Sharma, J.S. Tawale, S.K. Srivastava, Facile synthesis and tailoring the structural and photoluminescence properties of ZnO nanoparticles via annealing in air atmosphere, Mater. Today Commun. 32 (2022) 103845, https://doi.org/10.1016/j.mtcomm.2022.103845.

[17] M. Suja, S.B. Bashar, M.M. Morshed, J. Liu, Realization of Cu-doped p-type ZnO thin films by molecular beam epitaxy, ACS Appl. Mater. Interfaces 7 (16) (2015) 8894–8899, https://doi.org/10.1021/acsami.5b01564.

[18] N. Hadi, G. Morteza, S. Hamid, Photocatalysts capability of bentonite-ZnO nanocomposite synthesized by solution combustion in Ciprofloxacin degradation, J. Ultrafine Grained Nanostruct. Mater. 56 (1) (2023) 1–10, https://doi.org/10.22059/jufgnsm.2023.01.01.

[19] S. Bachir, K. Azuma, J. Kossanyi, P. Valat, J.C. Ronfard-Haret, Photoluminescence of polycrystalline zinc oxide co-activated with trivalent rare earth ions and lithium. Insertion of rare-earth ions into zinc oxide, J. Lumin. 75 (1) (1997) 35–49, https://doi.org/10.1016/S0022-2313(97)00093-8.

[20] M. Achehboune, M. Khenfouch, I. Boukhoubza, I. Derkaoui, L. Leontie, A. Carlescu, B.M. Mothudi, I. Zorkani, A. Jorio, Optimization of the luminescence and structural properties of Er-doped ZnO nanostructures: effect of dopant concentration and excitation wavelength, J. Lumin. 246 (2022) 118843, https://doi.org/10.1016/j.jlumin.2022.118843.

[21] M. Peres, J. Wang, M.J. Soares, A. Neves, T. Monteiro, E. Rita, E. Alves, PL studies on ZnO single crystals implanted with thulium ions, Superlattice. Microst. 36 (4–6) (2004) 747–753, https://doi.org/10.1016/j.spmi.2004.09.031.

[22] T. Monteiro, A.J. Neves, M.C. Carmo, M.J. Soares, M. Peres, E. Alves, U. Wahl, Optical and structural analysis of bulk ZnO samples undoped and rare earth doped by ion implantation, Superlattice. Microst. 39 (1–4) (2006) 202–210, https://doi.org/10.1016/j.spmi.2005.08.043.

[23] R. Pérez-Casero, A. Gutiérrez-Llorente, W. Seiler, R.M. Defourneau, D. Defourneau, E. Millon, B. Viana, Er-doped ZnO thin films grown by pulsed-laser deposition, J. Appl. Phys. 97 (5) (2005), https://doi.org/10.1063/1.1858058.

[24] S. Iwan, S. Bambang, J.L. Zhao, S.T. Tan, H.M. Fan, L. Sun, X.W. Sun, Green electroluminescence from an n-ZnO: Er/p-Si heterostructured light-emitting diode, Phys. B Condens. Matter 407 (14) (2012) 2721–2724, https://doi.org/10.1016/j.physb.2012.03.072.

[25] S. Nam, A.D. French, B.D. Condon, M. Concha, Segal crystallinity index revisited by the simulation of X-ray diffraction patterns of cotton cellulose Iβ and cellulose II, Carbohydr. Polym. 135 (2016) 1–9, https://doi.org/10.1016/j.carbpol.2015.08.035.

[26] S.B. V, S. Bhat, K.G. Naik, Studies on n-ZnO/p-Si heterojunction fabricated by hydrothermal method, AIP Conf. Proc. 1665 (1) (2015), https://doi.org/10.1063/1.4917788.

[27] S. Kinra, M.P. Ghosh, S. Mohanty, R.K. Choubey, S. Mukherjee, Manganese ions substituted ZnO nanoparticles: synthesis, microstructural and optical properties, Phys. B Condens. Matter 627 (2022) 413523, https://doi.org/10.1016/j.physb.2021.413523.

[28] S.T. Khlayboonme, W. Thowladda, Impact of Al-doping on structural, electrical, and optical properties of sol-gel dip coated ZnO: Al thin films, Mater. Res. Express 8 (7) (2021) 076402, https://doi.org/10.1088/2053-1591/ac113d, 6402.

[29] A. Khorsand Zak, J. Esmaeilzadeh, A.M. Hashim, X-ray peak broadening and strain-driven preferred orientations of pure and Al-doped ZnO nanoparticles prepared by a green gelatin-based sol-gel method, J. Mol. Struct. 1303 (2024) 137537, https://doi.org/10.1016/j.molstruc.2024.137537.

[30] Q. Chen, X. Li, Y. Wang, J. Wang, L. Chang, Y. Zhang, H. Ma, X. Jia, Optimization of thermoelectric properties of Al-doped $Zn_{1-x}Al_xO$ under high pressure and high temperature, J. Alloys Compd. 886 (2021) 161200, https://doi.org/10.1016/j.jallcom.2021.161200.

[31] A. Sridhar, P. Sakthivel, K. Saravanakumar, R.K. Sankaranarayanan, Dual doping effect of Ag+ & Al3+ on the structural, optical, photocatalytic properties of ZnO nanoparticles, Applied Surface Science Advances 13 (2023) 100382, https://doi.org/10.1016/j.apsadv.2023.100382.

[32] M. Yazdanbakhsh, I. Khosravi, E.K. Goharshadi, A. Youssefi, Fabrication of nanospinel $ZnCr_2O_4$ using sol–gel method and its application on removal of azo dye from aqueous solution, J. Hazard Mater. 184 (1) (2010) 684–689, https://doi.org/10.1016/j.jhazmat.2010.08.092.

[33] U. Jinendra, D. Bilehal, B.M. Nagabhushana, A.P. Kumar, M. Afzal, C. Shivamallu, S.S. Majani, S.P. Kollur, Synthesis, characterization, and photoluminescence investigations of Al/Co-doped ZnO nanopowder, J. Mol. Struct. 1305 (2024) 137701, https://doi.org/10.1016/j.molstruc.2024.137701.

[34] I. Elhamdi, H. Souissi, O. Taktak, J. Elghoul, S. Kammoun, E. Dhahri, B.F.O. Costa, Experimental and modeling study of ZnO:Ni nanoparticles for near-infrared light emitting diodes, RSC Adv. 12 (21) (2022) 13074–13086, https://doi.org/10.1039/D2RA00452F.

[35] A. Sharma, R.K. Khangarot, K.P. Misra, R.D.K. Misra, S. Chattopadhyay, P.D. Babu, N. Halder, Band gap reduction and quenching of pd exchange interaction in DOI 10.1088/1402-4896/abf8ea. sol-gel derived Zn (Al, Cu) O nanostructures, Phys. Scripta 96 (7) (2021) 075803.

[36] G.A. Waychunas, Luminescence spectroscopy, Rev. Mineral. Geochem. 78 (1) (2014) 175–217, https://doi.org/10.2138/rmg.2014.78.5.

[37] Y. Dai, G. Xie, X. Jia, B. Guo, J.R. Gong, Surface charge recombination matters for single-versus polycrystalline catalysts in the case study of hematite photoanodes, Appl. Surf. Sci. 610 (2023) 155501, https://doi.org/10.1016/j.apsusc.2022.155501.

[38] P. Kumari, A. Srivastava, R.K. Sharma, A. Saini, D. Sharma, J.S. Tawale, S.K. Srivastava, Facile synthesis and tailoring the structural and photoluminescence properties of ZnO nanoparticles via annealing in air atmosphere, Mater. Today Commun. 32 (2022) 103845, https://doi.org/10.1016/j.mtcomm.2022.103845.

[39] V. Sivakumar, D. Sivaganesh, J.N. Gopal, M. Muthuvinayagam, J.M. Kim, P.K. Kannan, S. Saravanakumar, Enhancement of intrinsic green emission in phase pure ZnO. Physica B, Condensed Matter 644 (2022) 414155, https://doi.org/10.1016/j.physb.2022.414155.

[40] M. Suja, S.B. Bashar, M.M. Morshed, J. Liu, Realization of Cu-doped p-type ZnO thin films by molecular beam epitaxy, ACS Appl. Mater. Interfaces 7 (16) (2015) 8894–8899, https://doi.org/10.1021/acsami.5b01564.

[41] H.A. Varudkar, G. Umadevi, P. Nagaraju, J.S. Dargad, V.D. Mote, Fabrication of Al-doped ZnO nanoparticles and their application as a semiconductor-based gas sensor for the detection of ammonia. Journal of Materials Science, Materials in Electronics 31 (15) (2020) 12579–12585, https://doi.org/10.1007/s10854-020-03808-7.

[42] B. Huang, Doping of RE ions in the 2D ZnO layered system to achieve low-dimensional upconverted persistent luminescence based on asymmetric doping in ZnO systems, Phys. Chem. Chem. Phys. 19 (20) (2017) 12683–12711, https://doi.org/10.1039/C7CP01623A.

[43] M.A. Majeed Khan, M. Wasi Khan, M. Alhoshan, M.S. AlSalhi, A.S. Aldwayyan, Influences of Co doping on the structural and optical properties of ZnO nanostructured, Appl. Phys. A 100 (1) (2010) 45–51, https://doi.org/10.1007/s00339-010-5840-8.

[44] A. Naseri, M. Samadi, N.M. Mahmoodi, A. Pourjavadi, H. Mehdipour, A.Z. Moshfegh, Tuning composition of electrospun ZnO/CuO nanofibers: toward controllable and efficient solar photocatalytic degradation of organic pollutants, J. Phys. Chem. C 121 (6) (2017) 3327–3338, https://doi.org/10.1021/acs.jpcc.6b10414.

[45] N. Ahmadpour, M.H. Sayadi, S. Sobhani, M. Hajiani, Photocatalytic degradation of model pharmaceutical pollutant by novel magnetic TiO_2@$ZnFe_2O_4$/Pd nanocomposite with enhanced photocatalytic activity and stability under solar light irradiation, J. Environ. Manag. 271 (2020) 110964, https://doi.org/10.1016/j.jenvman.2020.110964.
[46] U. inendra, D. Bilehal, B.M. Nagabhushana, A.P. Kumar, Adsorptive removal of Rhodamine B dye from aqueous solution by using graphene–based nickel nanocomposite, Heliyon 7 (4) (2021) e06851, https://doi.org/10.1016/j.heliyon.2021.e06851.
[47] N.K. Mondal, S. Kar, Potentiality of banana peel for removal of Congo red dye from aqueous solution: isotherm, kinetics and thermodynamics studies, Appl. Water Sci. 8 (6) (2018) 157, https://doi.org/10.1007/s13201-018-0811-x.
[48] J. Raeder, D. Larson, W. Li, E.L. Kepko, T. Fuller-Rowell, OpenGGCM simulations for the THEMIS mission, Space Sci. Rev. 141 (1) (2008) 535–555, https://doi.org/10.1007/s11214-008-9421-5.
[49] U. Jinendra, B.M. Nagabhushana, D. Bilehal, M. Iqbal, R.G. Amachawadi, C. Shivamallu, S.P. Kollur, Encapsulated Co-ZnO nanospheres as degradation tool for organic pollutants: synthesis, morphology, adsorption and photo luminescent investigations, Spectrochim. Acta Mol. Biomol. Spectrosc. 299 (2023) 122879, https://doi.org/10.1016/j.saa.2023.122879.
[50] M. Turabik, Adsorption of basic dyes from single and binary component systems onto bentonite: simultaneous analysis of Basic Red 46 and Basic Yellow 28 by first order derivative spectrophotometric analysis method, J. Hazard Mater. 158 (1) (2008) 52–64, https://doi.org/10.1016/j.jhazmat.2008.01.033.
[51] P. Roy, N.K. Mondal, K. Das, Modeling of the adsorptive removal of arsenic: a statistical approach, J. Environ. Chem. Eng. 2 (1) (2014) 585–597, https://doi.org/10.1016/j.jece.2013.10.014.
[52] U. Jinendra, D. Bilehal, B.M. Nagabhushana, K.S. Jithendra Kumara, S.P. Kollur, Nano-catalytic behavior of highly efficient and regenerable mussel-inspired Fe_3O_4@CFR@GO and Fe_3O_4@CFR@TiO_2 magnetic nanospheres in the reduction of Evans blue dye, Heliyon 7 (1) (2021) e06070, https://doi.org/10.1016/j.heliyon.2021.e06070.